PHYSIOLOGY

Metabolic rewiring of the hypertensive kidney

Markus M. Rinschen[1,2], Oleg Palygin[3], Carlos Guijas[1], Amelia Palermo[1], Nicolas Palacio-Escat[4,5,6], Xavier Domingo-Almenara[1], Rafael Montenegro-Burke[1], Julio Saez-Rodriguez[4,5,7], Alexander Staruschenko[3,8]*, Gary Siuzdak[1]*

Hypertension is a persistent epidemic across the developed world that is closely associated with kidney disease. Here, we applied a metabolomic, phosphoproteomic, and proteomic strategy to analyze the effect of hypertensive insults on kidneys. Our data revealed the metabolic aspects of hypertension-induced glomerular sclerosis, including lipid breakdown at early disease stages and activation of anaplerotic pathways to regenerate energy equivalents to counter stress. For example, branched-chain amino acids and proline, required for collagen synthesis, were depleted in glomeruli at early time points. Furthermore, indicators of metabolic stress were reflected by low amounts of ATP and NADH and an increased abundance of oxidized lipids derived from lipid breakdown. These processes were specific to kidney glomeruli where metabolic signaling occurred through mTOR and AMPK signaling. Quantitative phosphoproteomics combined with computational modeling suggested that these processes controlled key molecules in glomeruli and specifically podocytes, including cytoskeletal components and GTP-binding proteins, which would be expected to compete for decreasing amounts of GTP at early time points. As a result, glomeruli showed increased expression of metabolic enzymes of central carbon metabolism, amino acid degradation, and lipid oxidation, findings observed in previously published studies from other disease models and patients with glomerular damage. Overall, multilayered omics provides an overview of hypertensive kidney damage and suggests that metabolic or dietary interventions could prevent and treat glomerular disease and hypertension-induced nephropathy.

INTRODUCTION

According to the American Heart Association, 116.4 million (46%) adults in the United States have hypertension (*1*). Although long-term high salt intake increases the risk for hypertension and associated cardiovascular and chronic kidney disease (*2*, *3*), the specific mechanisms underlying salt-induced changes in blood pressure and kidney injury are poorly understood. Hypertension causes one-third of chronic kidney disease, but its prevention and treatment are largely unmet. Kidney diseases affect more than 1 of 10 persons in developed countries, potentiate cardiovascular risk, and lead to a large socioeconomic burden.

Kidneys regulate body metabolism by filtering urine through the glomerulus and then reabsorbing nutrients, a role that makes them a central metabolic organ. The glomerulus is the filtration unit of the kidney that is frequently viewed as a passive filter that limits protein passage through size exclusion yet remains permeable for small molecules. Hypertension is thought to damage glomeruli of the kidney, resulting in increased protein in the urine, a hallmark of kidney disease (*4*).

To investigate kidney disease, we used a multi-omic strategy, integrating metabolomics, phosphoproteomics, and proteomics. Among all omics dimension, the metabolome is the most downstream and its relevance for the understanding (and regulation of) physiological mechanisms is only beginning to be understood. For example, the metabolome modulates phenotypes by interacting with the other omic levels including the genome, transcriptome, proteome (*5*, *6*), and the posttranslationally modified proteome (*7*). Here, we investigated in a well-established model of hypertension and proteinuria [the Dahl salt-sensitive (DSS) rat] the metabolome changes that preceded the proteome and phosphoproteome in a subtissue-specific manner. This naturally occurring model of salt-sensitive hypertension recapitulates many aspects of progressive human hypertension, providing key insight into mechanisms underlying salt sensitivity (*8*). In this study, we uncovered key pathways and mechanisms that were controlled by the metabolome and were related to physiological functions and omic perturbations not commonly thought to be metabolically controlled, providing a window into hypertension-induced kidney molecular rewiring and its categorization as a metabolic disease.

RESULTS

Untargeted metabolome analysis of DSS rats reveals lipid breakdown and branched-chain amino acids in glomeruli, but not in the tubules

DSS rats develop hypertension and salt-induced nephropathy when placed on a high-salt diet. The effect of salt on blood pressure can be described in two phases. An initial increase in blood pressure observed in the first week on a high-salt diet is followed by the subsequent rise of blood pressure that is accompanied by renal injury. Therefore, we performed an untargeted metabolome analysis of glomeruli and tubules freshly isolated from DSS rats when they were switched from normal (0.4%) to high-salt (4%) diets for 7 and 21 days, respectively. Upon induction of hypertension, we found an increase in albuminuria

[1]Center for Metabolomics and Mass Spectrometry, The Scripps Research Institute, La Jolla, CA 92122, USA. [2]Department II of Internal Medicine and Center for Molecular Medicine, University of Cologne, Cologne 50931, Germany. [3]Department of Physiology, Medical College of Wisconsin, Milwaukee, WI 53226, USA. [4]COMBINE-Joint Research Center for Computational Biomedicine RWTH Aachen University, Aachen 52074, Germany. [5]Institute of Computational Biomedicine, Bioquant, Faculty of Medicine and Heidelberg University Hospital, Heidelberg University, Heidelberg 69120, Germany. [6]Faculty of Biosciences, University of Heidelberg, Heidelberg 69120, Germany. [7]Molecular Medicine Partnership Unit (MMPU), European Molecular Biology Laboratory and Heidelberg University, Heidelberg 69120, Germany. [8]Clement J. Zablocki VA Medical Center, Milwaukee, WI 53295, USA.
*Corresponding author. Email: staruschenko@mcw.edu (A.S.); siuzdak@scripps.edu (G.S.)

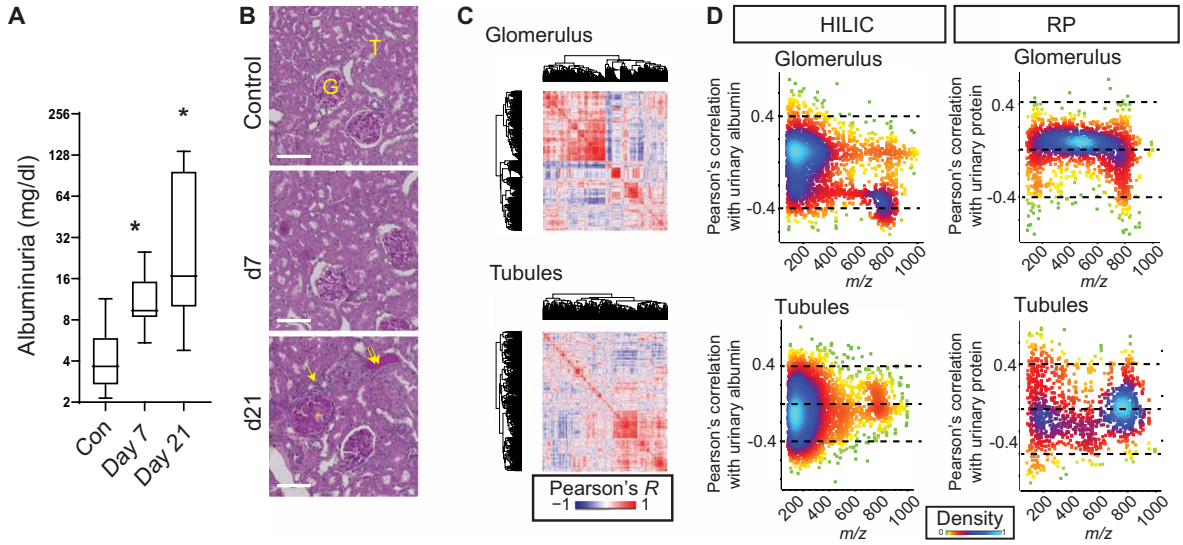

Fig. 1. Tissue-specific phenotyping and untargeted metabolomic analysis of salt-sensitive rats reveals a distinct glomerular response to hypertension. (**A**) Albuminuria in DSS rats after 1 or 3 weeks on a high-salt diet. Data are generated from $n = 5$ rats for each group. A significant increase in albuminuria was observed [$P < 0.05$ by analysis of variance (ANOVA)]. (**B**) Kidney histology of DSS rats after 1 or 3 weeks on a high-salt diet. Images are representative of $n = 3$ rats for each group. Scale bar, 100 μm. (**C**) Overview of highly abundant metabolites in the tubular and glomerular compartments from DSS rats after 1 or 3 weeks on a high-salt diet obtained through untargeted metabolomic analysis as annotated by the MISA (METLIN-guided in-source fragment annotation) algorithm. (**D**) Pearson's correlation of XC-MS annotated features with albuminuria in the same rat. The dashed line indicates a Pearson's correlation coefficient of 0.4 or −0.4. Each dot presents a feature. The dataset of two different chromatographic analyses [hydrophilic interaction liquid chromatography (HILIC) and reversed-phase (RP) chromatography] is presented.

(Fig. 1A). Tissue or glomeruli damage was not detectable at week 1 (Fig. 1B). In contrast, at week 3, strong albuminuria was observed and substantial tissue damage affected both the cortex tubular tissue and the glomeruli. Untargeted metabolomic profiles were generated from both the glomeruli and the cortical fraction, which mainly contained proximal tubules. We performed metabolite extraction and analysis through ultraperformance liquid chromatography/mass spectrometry (UPLC/MS) experiments for both tissues. In-source fragment annotation using the METLIN-guided in-source fragment annotation (MISA) algorithm identified 900 putative metabolite features that were further hierarchically clustered using Euclidean distance (*9*). The correlation matrix of features across the animals of the study was different between tubule and glomerular datasets (Fig. 1C). Metabolomic analysis also showed that high mass/charge ratio (*m/z*) features (such as complex lipids) around 600 to 800 Da were generally negatively correlated with proteinuria detected in the same rat (Fig. 1D). Subsequently, metabolites from tubules and glomeruli from rats on the high-salt diets after days 7 and 21 were compared to those from control animals (data file S1 and fig. S5). Untargeted analysis revealed that proline and the branched-chain amino acid leucine were decreased in glomeruli, but not tubules (Fig. 2A). In tubules, these amino acids were not regulated, but other amino acids such as aromatic (phenylalanine), cationic, and polar amino acids were decreased. Quantification of amino acid metabolites revealed a decrease in the branched-chain metabolite acetylleucine, acetylvaline, and acetylproline in the glomerulus that was not present in the tubules of the same rats (Fig. 2B). We observed increased glucose 6-phosphate and decreased glyceraldehyde 3-phosphate after 3 weeks that was again present only in glomeruli, but not in tubules (Fig. 2C). In addition, the free fatty acids stearic acid, oleic acid, and linoleic acid, as well as acylcarnitines, were decreased after 3 weeks of high salt, again chiefly in glomeruli (Fig. 2D). Other metabolites, such as choline and creatinine, were strongly regulated in tubules, but not in glomeruli (Fig. 2E). Thus, untargeted metabolite analysis suggested alterations in branched-chain amino acid, proline, and lipid metabolism in glomeruli, whereas tubules largely showed decreased amino acid content.

Targeted metabolome analysis reveals oxidative stress and energy-equivalent metabolite depletion predominantly in glomeruli

A targeted metabolic analysis of glomeruli and tubules was next performed. Glomeruli showed decreases in products of central carbon metabolism including citrate/isocitrate, α-ketoglutarate, and succinate that occurred at the early time point, suggesting a general depletion of tricarboxylic acid (TCA) cycle metabolites. These changes were not significantly altered in tubules despite a similar trend in many TCA cycle metabolites (Fig. 3A). The pyruvate/lactate ratio was not changed in either tissue (Fig. 3B). Both the $NADH/NAD^+$ and GTP (guanosine triphosphate)/GDP (guanosine diphosphate) ratios were decreased only in glomeruli after day 7 (Fig. 3, C and D). The adenosine triphosphate (ATP)/adenosine diphosphate (ADP) ratio was significantly reduced at day 21 (Fig. 3E). In addition, the oxidized lipids 5-hydroxyeicosatetraenoic acid (5-HETE), 9-HETE, and 15-HETE were increased in glomeruli, but not in tubules (Fig. 3F). These results suggest that in hypertensive rats, metabolic stress is present chiefly in glomeruli, but not in tubules (data file S2).

Depleted metabolites trigger mTOR and AMPK rewiring

The observed metabolomic changes could directly contribute to altered phosphoprotein-dependent signaling. Therefore, MS-based phosphoproteomic analysis was performed on the same animal model, specifically on glomeruli. Ninety phosphopeptides out of the

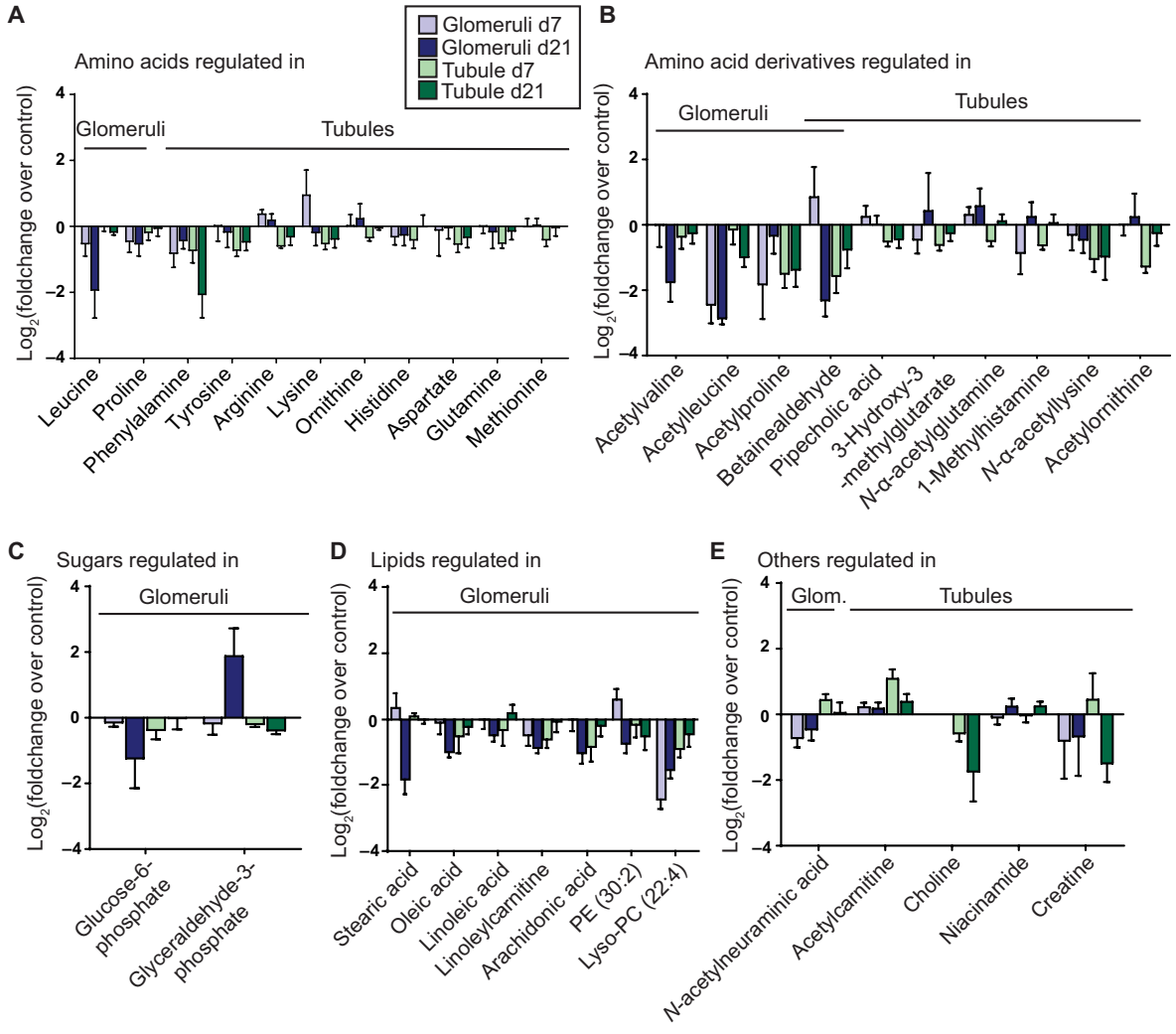

Fig. 2. Untargeted metabolomic analysis of the kidney cortex and the kidney glomeruli. The indicated amino acids (**A**), amino acid derivatives (**B**), sugars (**C**), lipids (**D**), and other metabolites (**E**) obtained through untargeted metabolomic analysis of DSS rats after 1 or 3 weeks on a high-salt diet. For (A) to (E), data are from $n = 6$ rats for each group. The bars indicate significance based on a Kruskal-Wallis test of signal intensities. Data are presented as mean ratios (fold change over control) ± SEM.

~3000 quantified phosphosites were regulated at day 7, but only 5 phosphopeptides were regulated at day 21 (Fig. 4, A and B, and data file S3). After 1 week, we found a decrease in the phosphorylation of an inhibiting site of Prkaa2 [the catalytic subunit of adenosine monophosphate (AMP)–activated protein kinase (AMPK)], suggesting activation of AMPK, and in the phosphorylation of an activating site of raptor (RPTOR), a protein that activates mammalian target of rapamycin complex 1 (mTORC1). These results suggested that metabolite-controlled signaling occurs, because a decreased ADP/ATP ratio (Fig. 3E) would be expected to activate AMPK (as indicated by decreased phosphorylation at Ser^{491}), and decreased leucine inhibits mTOR, as indicated by a reduced phosphorylation of RPTOR at Ser^{722}. Quantification of the temporal trajectories of the phosphoproteomic perturbations showed that two clusters of phosphopeptides were increased in a manner that correlated with hypertensive damage. Position-weighted matrices of amino acid frequency over the UniProt background suggested a preference of basophilic sites in this group (Fig. 4C). For a more accurate annotation, we performed enrichment analysis that uncovered an overrepresentation of motifs for AMPK and for related kinases such as glycogen synthase kinase (GSK) and HMG-CoA-reductase kinase, the kinase that inhibits the key enzyme in cholesterol synthesis (Fig. 4C). Last, we performed quantitative phosphoproteomic modeling of the two kinases with the most evidence for activation, namely, Raptor and AMPK, using the PHONEMeS algorithm (Fig. 5) (*10*). The modeling showed a stronger preference for these kinases to target functional cytoskeletal parts at early time points. Targets of the metabolic signaling were the GTP-binding protein RCC1 at Ser^{11}, resulting in enhanced activity (*11*); cofilin at Ser^{3}, a site involved in actin bundling; and 3-phosphoinositide-dependent protein kinase-1 (PDK1) at an activating site, suggesting that metabolic signaling controls key pathophysiological pathways in the glomerulus.

Proteomic analysis shows that alterations in metabolite-processing enzymes are a conserved feature in glomerular disease

We then asked whether the observed changes were mainly due to changes in protein expression. Proteomic analysis of the same samples revealed that protein abundance was altered to a lesser extent compared

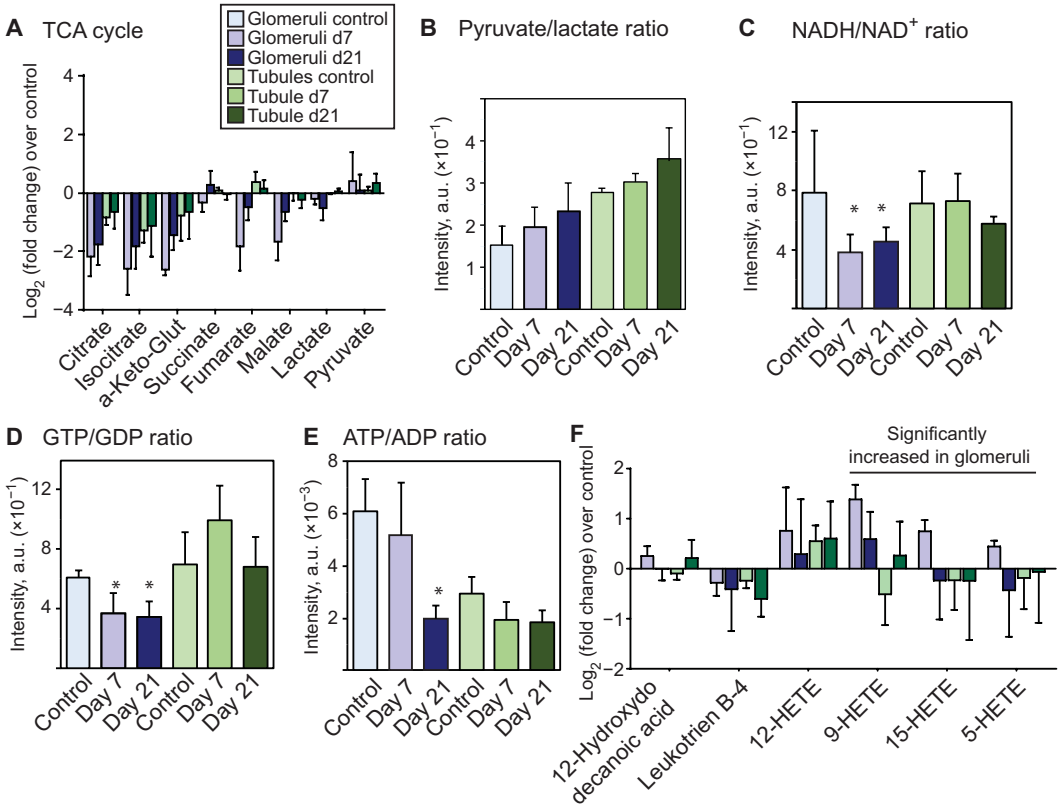

Fig. 3. Targeted metabolomic analysis of salt-sensitive hypertensive rats reveals metabolic dysfunction in the glomeruli. (**A** to **F**) Analysis of TCA cycle metabolites (A), the pyruvate-lactate ratio (B), the NADH/NAD$^+$ ratio (C), the GTP/GDP ratio (D), the ATP/ADP ratio (E), and the oxidized lipids 5-HETE, 9- HETE, and 15-HETE (F). The color-coding scheme in (A) applies to (B) to (F). *$P < 0.05$ by one-way ANOVA with Dunnett's post test. For (A) to (F), data are presented as means ± SEM from $n = 5$ rats for each group.

to phosphorylation, suggesting that phenotypes were modulated more by changes in metabolic signaling than those in protein abundance. We found that 90 proteins were altered in abundance in a statistically significant manner, including collagen type 6, which is proline rich. Complement proteins were not strongly increased in abundance in the glomerulus, which was confirmed by complement staining (fig. S1A). Proteins in the branched-chain amino acid catabolic pathway were increased in abundance, including the branched-chain aminotransferase BCAT2 and hexokinase 1 at week 3 (fig. S1, B and C, and data file S4). Two guanosine triphosphatases (GTPases) increased in abundance, namely, OPA1, a dynamin-like mitochondrial Rho GTPase, and Arpc1b (fig. S1A). The adenosine triphosphatase (ATPase) Asna and the myosin ATPase Myo1b showed increased expression at week 3. The GTP-AMP phosphotransferase AK3 was increased in abundance at week 1. ABCD3, a transporter involved in the transport of branched-chain fatty acids with ATPase activity, was also increased. In addition, the increased abundance of HK1 (at week 3) was preceded by decreases in glucose-6-phosphate at week 1. At the same time, proteins involved in responses to oxidative stress were induced, such as MPST1, a mercaptopyruvarte sulfurtransferase. Hierarchical clustering followed by trajectory analysis revealed that extracellular matrix proteins were increased after 3 weeks of hypertension. We next performed metabolic modeling using a Kyoto Encyclopedia of Genes and Genomes (KEGG) pathway–limited mapping and a network-reaction mapping using MetExplore. Statistical mapping on pathview showed that β-oxidation pathways and branched-chain amino acid catabolism were increased (Fig. 6, A and B, and fig. S2, A and B), consistent with metabolomic data showing a decrease in stearic acid, acylcarnitines, and branched-chain amino acids (Fig. 1, E and H). We also mapped fold changes on the MetExplore network tool that links metabolomic data with genome-scale networks (*12*), which suggested that the branched-chain amino acid leucine was a critical carbon source in the system, providing an explanation for the activation of metabolic signaling, including inhibited mTOR signaling (fig. S3).

Because widespread molecular rewiring occurred together with or after the metabolite changes, we asked whether additional proteins—beyond canonical pathways—could be regulated by metabolites. We used the IBM Watson natural language processing (NLP) platform to identify proteins that were associated with or activated by the known metabolomic perturbations (Fig. 6C) (*13*). We focused on proteins that were regulated by multiple metabolites, according to the IBM Watson NLP. Out of the dysregulated proteins, we found that the activity (as indicated by activating phosphorylation) or abundance of eight proteins could be explained by the metabolic perturbations. These proteins included vascular endothelial growth factor A (VEGF-A), transforming growth factor–β (TGF-β), and cell adhesion proteins. The NLP prediction also included the regulation of mTOR and AKT as observed at the phosphoproteomic level. For all proteins, the direction of regulation between metabolites and proteins was consistent (data file S5).

Last, to determine whether the observed signatures were conserved across models of albuminuria, including human samples, we compiled previously published glomerular proteomic data from different models

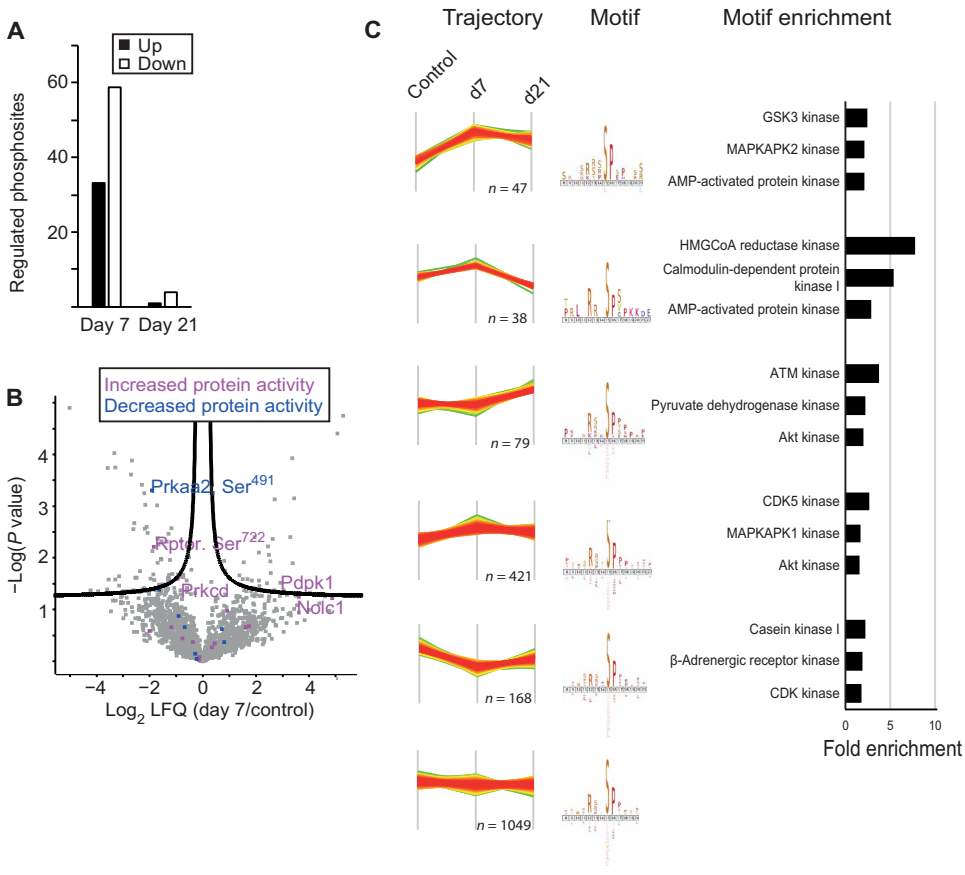

Fig. 4. Phosphoproteomic analysis reveals metabolome-dependent phosphoproteome rewiring after 1 week, but not 3 weeks. (**A**) Overview of the number of phosphosites showing up-regulation ("up") or down-regulation ("down"). (**B**) Volcano plot of phosphosite intensity quantification after 1 week of hypertension. $n = 5$ rats per group. Significance of the comparison day 7 over control (–log P value of a two-tailed t test) is plotted against the $\log_2$ ratio of the label-free intensities (LFQ). The dashed lines indicate significance after correcting for multiple testing. The color key indicates activating and inhibiting sites (based on phosphosite.org annotation). (**C**) Trajectory analysis of high-confidence phosphorylation sites. For (A) to (C), data are from $n = 4$ rats for each group. "n" in the figures indicate the number of proteins in each cluster.

of proteinuria. The data included animal models of proteinuria, including the proteinuric rat induced by puromycin-aminonucleoside (PAN) and glomerular proteomic data from mice treated with doxorubicin (*14*–*17*). We also included primary urinary cells from a patient with an *ACTN4* mutation that caused proteinuria and focal segmental glomerulosclerosis (FSGS) (*17*). Homologene groups were used to determine the conserved proteins, and we converted fold changes into z scores, which we further processed computationally (data file S6). Initially, protein data from animal models with similar proteome coverage were assessed. Hierarchical clustering was performed to identify signatures that were common across all animal models (fig. S4A). We found two clusters that were increased in glomeruli of doxorubicin-treated mice, as well as in the hypertensive rats (fig. S4B). Both clusters had more than 90% of proteins that were determined to have metabolic activity in any pathway [as defined by Gene Ontology (GO) mapping] (fig. S4C). The clusters showed overrepresentation of expression of enzymes in glycolytic, branched-chain amino acid metabolism, and β-oxidative pathways (fig. S4, D and E). Most of the reduced proteins were expressed in a podocyte-specific fashion as determined by our previous atlas of podocyte-specific proteins in mice (*15*), suggesting that these changes occurred in the podocytes. Human primary cells from FSGS patients showed similar patterns of changes in protein expression (fig. S4F).

DISCUSSION

Our analysis of a rat model of hypertensive kidney damage provides deeper understanding of the metabolomic, proteomic, and phosphoproteomic changes that occur in this disease. The study was designed to catch both hypertension-dependent perturbations (1 week after the induction of hypertension) and changes caused by tissue remodeling (3 weeks after the induction of hypertension). Metabolic insults occurred in glomeruli, which comprise 2% of the kidney, whereas tubules showed changes that were chiefly related to altered amino acid handling. The early findings in the glomeruli were depletion of energy equivalents, involving specifically GTP, lipid breakdown, and depletion of distinct amino acid species. These resulted in increased AMPK signaling and phosphorylation-dependent signaling to the cytoskeleton and changes in the proteins that regulate the metabolites. The integrated view of this dataset generates the following insights into metabolic rewiring.

In terms of energy equivalents, hypertensive insults resulted in an early decrease of GTP and NADH, followed by a decrease in ATP (Fig. 3, C to E). The trajectory was consistent with the stress-induced induction of ATPases and GTPases that may be necessary to maintain the transport if membranes are endocytosed and subjected to autophagy (fig. S1, B and C). Small GTPases are highly podocyte-enriched proteins (such as RhoA and Rac1) that are key mediators of podocyte injury, and induction of these proteins may increase actin-branched motility. The dataset contained increased expression of two increased GTPases, namely, OPA1, a dynamin-like mitochondrial Rho GTPase, and Arpc1, GTP-associated proteins (fig. S1A). The metabolome foreshadows their increased abundance (at week 3). The ATPase Asna, which regulates membrane reorganization, is increased after week 3, when ATP is decreased. Similarly, the myosin ATPase Myo1b is increased at week 3. The GTP-AMP phosphotransferase AK3 is increased at week 1, suggesting that ADP may be regenerated from GTP sources. ABCD3 is a transporter involved in the transport of branched-chain fatty acids that is also increased and has ATPase activity. Further analyses showed a consistent behavior: The increased abundance of HK1 (at week 3) is preceded by decreased abundances of the glucose-6-phosphate at week 1. MPST1, a mercaptopyruvarte sulfurtransferase, was increased at day 7, suggesting that the early

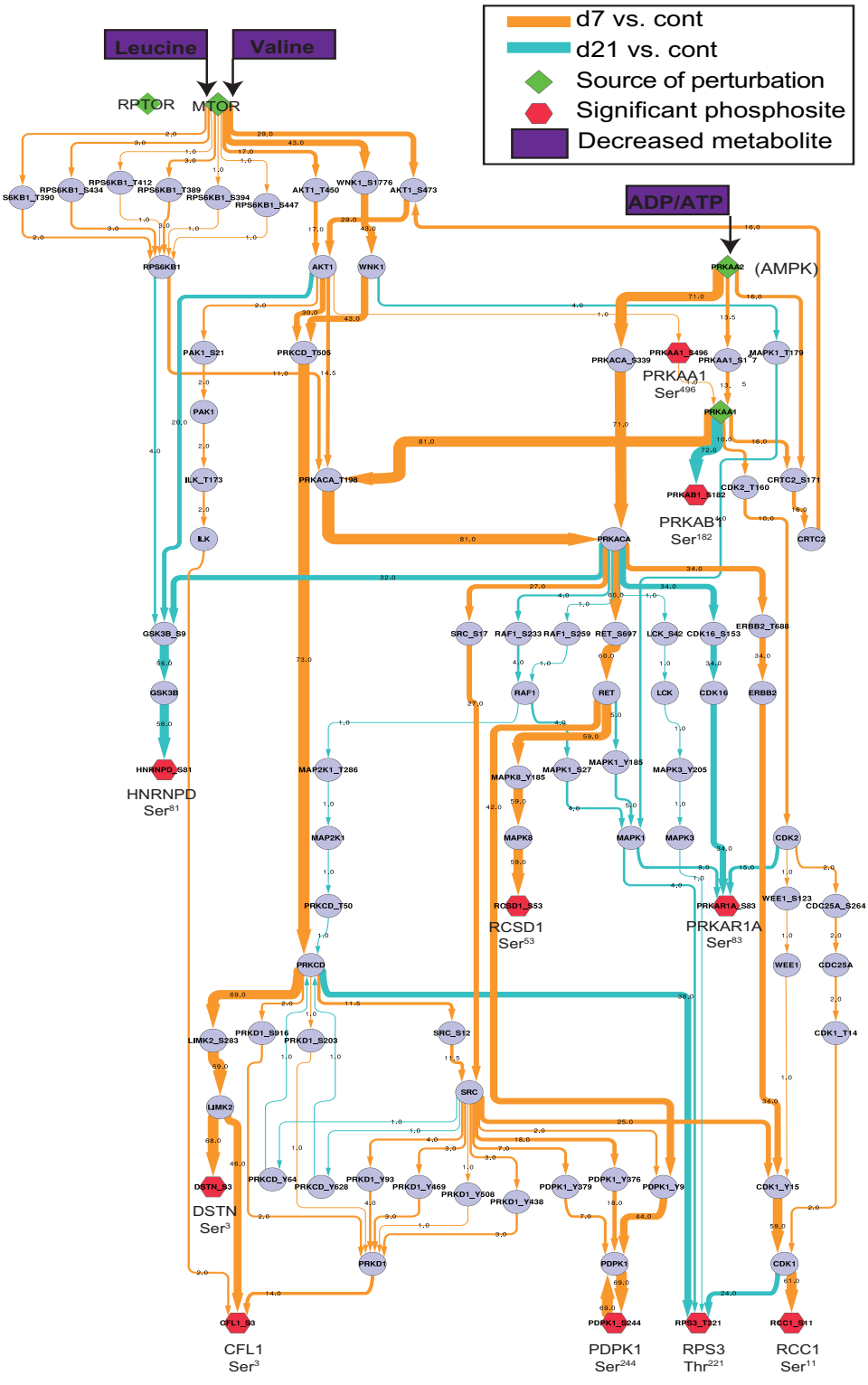

Fig. 5. Modeling of metabolite-dependent phosphoproteomic results using Phonemes. Thickness of arrows determines frequency of network observation during modeling. The purple nodes show statistically significantly regulated phosphorylation sites. The green nodes are the source of perturbation (AMPK and MTOR) based on metabolomic results (Fig. 4).

response also involves an antioxidative compound. These proteomic rewirings were conserved across several animal models of glomerular disease (fig. S4, A and B).

The data also revealed strong alteration in phospholipids and lipid species. Globally, putative phospholipid species (a population with masses of 600 to 800 Da) negatively correlated with albuminuria. In addition, β-oxidation enzymes, including the carnitine palmitoyltransferase Cpt1a, were increased in abundance (Figs. 1D and 6A). Both findings occurred in the glomeruli. Overall, membrane area is decreased in damaged "effaced" podocytes, which may be caused by increased lipid breakdown. This is suggested by the decrease of higher molecular lipid species (Fig. 1C) and the increase of oxolipids (Fig. 3F) (*18*). The reduction in *N*-acetylneuramine, a building block for the glycocalyx and a part of the membrane structure of the filtration barrier, may be consistent with this overall decrease in lipid membranes. In addition, we observed a decrease in LysoPC species and an increase in oxidized lipids (HETEs) that result from the breakdown of lipids. These lipids are usually proinflammatory (*19*), but some lipids, such as 15-HETE, are involved in resolving inflammation (*14*). Together, these findings are consistent with a reduction of membrane component phospholipid species.

The regulation of branched-chain amino acids and decrease in ATP correlated with alterations in the phosphoproteome caused by increased signaling of ATP-controlled kinases. AMPK phosphorylation was decreased at an inhibitory site (Fig. 4C). Raptor phosphorylation at an activating site that is targeted by many kinases, including mitogen-activated protein kinases (MAPKs) (*20*), was decreased, suggesting a metabolite-inhibited mTOR. On the basis of phosphoproteomic modeling, AMPK-mediated signaling chiefly controls the cytoskeleton: Phosphorylation of cofilin Ser^3, and of PDPK1 (a potentially druggable target downstream of AMPK and mTOR), was increased (Fig. 5). The general pattern of activation of mechanical components, such as components of the cytoskeleton and focal adhesion structures, is consistent with a phosphoproteomic study identifying AMPK substrates (*21*). This is of interest because virtually all disease processes that affect the glomerulus—whether genetic, humoral, chemical, or immunological in origin (*14*, *22*–*24*)—are associated with actin-related and mechanical processes. Therefore, it can be assumed that metabolic dysregulation, mediated chiefly by

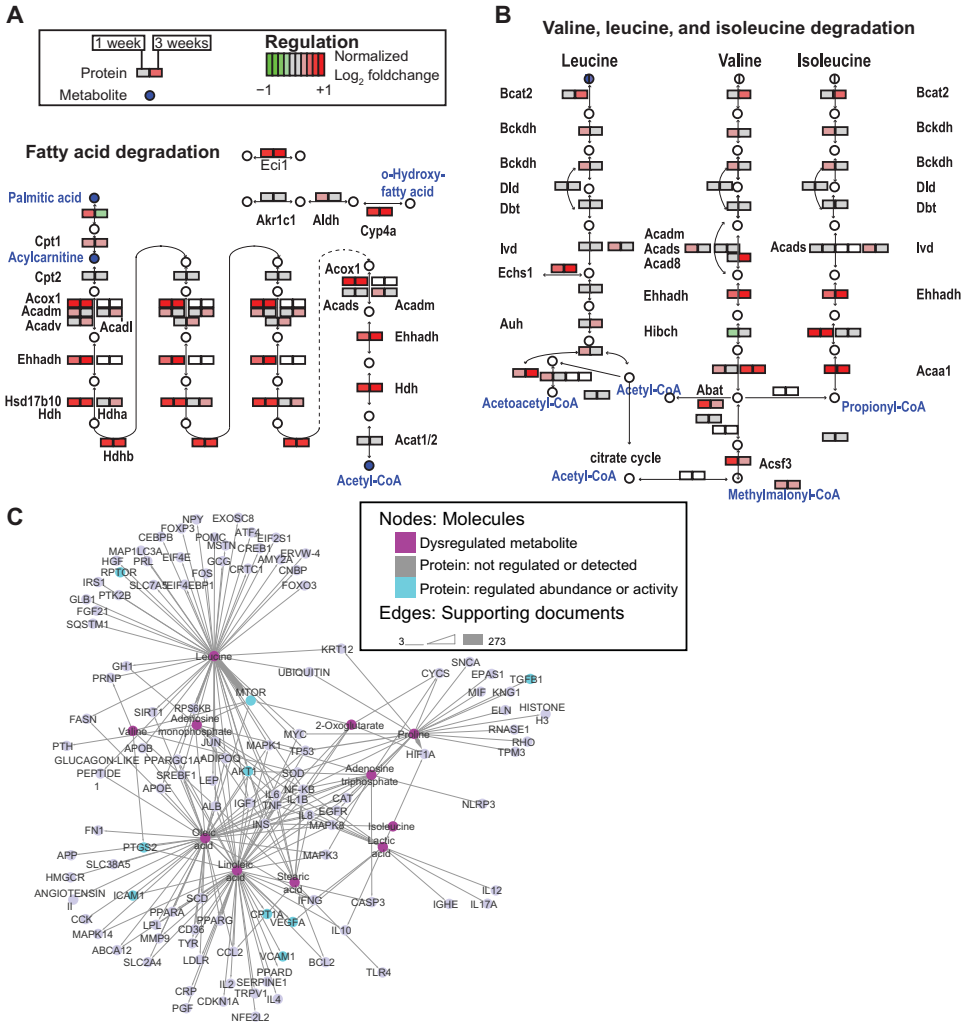

Fig. 6. Proteome-metabolome integration reveals increased abundance of enzymes involved in branched-chain amino acid catabolism, explaining decreased abundance of metabolites across models. (**A**) Mapping of protein and metabolite abundance on the KEGG pathway "fatty acid degradation." Logarithmized and normalized fold changes of abundance of metabolites and protein complexes were mapped on the KEGG pathway "fatty acid degradation." The left square shows the abundance at day 7, and the right square shows the abundance at day 21 as compared to control. Blue circles represent decreased metabolites. The entire maps are presented in fig. S4. The color code and figure legend also applies to (**B**). Members of the degrading enzyme complexes are labeled with their respective gene symbol. (B) Mapping of protein and metabolite abundance on the KEGG pathway "leucine, isoleucine and valine degradation." Panel legend is the same as in (A). (**C**) Metabolites were fed into an NLP program, and active relationships recognized by the program were depicted as a network.

AMPK and mTOR, could modulate or even trigger cytoskeleton alterations that cause podocyte injury.

Several serum analyses in chronic kidney disease in humans and rats have shown convincing links between amino acid metabolism, lipid composition, and oxidative stress (*25*–*29*). It is possible that similar changes contribute to the overall observed changes in tissue abundance observed in our study, for instance, the observed increased oxidative stress in glomeruli (Fig. 3, C to E).

Chakraborty *et al.* (*30*) reported that the ketone body hydroxybutyrate is decreased in the plasma of the DSS rat and that administration of the compound alleviates symptoms of hypertension and improves kidney tissue function. This mechanism was independent of the microbiota profile of the animals (*30*). This finding, together with our multiomics dataset, indicates that metabolic changes occur in glomeruli. If used by the kidney, ketone bodies would largely circumvent the processes observed here, reduce overall mitochondrial capacity, and provide sources of energy. In conclusion, the data demonstrate how the complex interplay between metabolites, protein phosphorylation, and proteins drives glomerular disease and raises the possibility for dietary interventions such as lipid-consuming, ketogenic diet and calorie restriction in humans to prevent the adverse effects of hypertension on the kidney.

MATERIALS AND METHODS

Animals

We used Rapp DSS rats (Ontology: SS/JrHsdMcwi, RS:0002576) that have been inbred for more than 50 generations at the Medical College of Wisconsin. This strain is a widely used and physiological model for the study of salt-sensitive hypertension and kidney injury (*31*–*33*). Male rats were obtained at weaning from colonies under controlled environmental conditions with parents and offspring. Rats were fed a purified AIN-76A rodent food (#D113755, Dyets Inc., Bethlehem, PA) containing 0.4% NaCl with water provided ad libitum. At 7 to 8 weeks of age, the salt content of the chow was either maintained at 0.4% (in the group fed a normal diet) or increased to 4.0% NaCl (Dyets Inc., #D113756) for either 7 or 21 days. Urine samples were collected for 24 hours using metabolic cages (40615; Laboratory Products) to measure albuminuria. Albuminuria was quantified using an Albumin Blue 580 (Molecular Probes) fluorescence assay. At the completion of the study, rats were surgically prepared by cardial perfusion, blood was flushed out using phosphate-buffered saline (PBS), and rats were humanely euthanized. The kidneys were removed, and part of the left kidneys was formalin-fixed and paraffin-embedded. Tissue sections were deparaffinized and stained with hematoxylin and eosin for analysis of kidney injury and glomerular morphology. The right and the other half of the left kidneys were removed and used for glomeruli and cortex fraction isolation, respectively. C3 immunohistochemistry was performed as described previously (*34*). Animal use and welfare procedures adhered to the National Institutes of Health (NIH) *Guide for the Care and Use of Laboratory Animals* following protocols reviewed and approved by the Medical College of Wisconsin Institutional Animal Care and Use Committee.

Isolation of the rat glomeruli

Kidneys of experimental SS rats were perfused to clear them of blood. Kidneys were removed and decapsulated as previously described (*31*). Briefly, the cortex was isolated, minced in small 1-mm^3 pieces, and mechanically strained through steel sieves with different mesh sizes. These procedures were performed in culture medium solution RPMI 1640 (Invitrogen Inc.). Collected glomeruli fractions were obtained by gentle centrifugation. All isolations were performed without the presence of bovine serum albumin to minimize protein contamination. The glomerular fraction contained between 90 and 98% glomeruli. After isolation, both glomeruli and cortical samples, which predominantly consist of tubule fractions, were snap-frozen and later used for metabolomic and proteomic analyses.

Metabolite extraction

Metabolites were extracted from snap-frozen tissue. About 10 mg of tissue was weighed in and stored on dry ice. Ice-cold methanol/acetonitrile/water (800 µl; 2:2:1, by volume) was added per 10 mg of tissue. Tissue was homogenized in a methanol/acetonitrile/water mixture using a bead-beating procedure (glass beads, for 30 s), and the homogenate was transferred to a new tube. The beads were washed with 200 µl of methanol/acetonitrile/water (2:2:1, by volume), and the homogenate was incubated for 2 hours at −20°C. The insoluble pellet was spun down by centrifugation at 4°C (16,000*g*, 20 min) in a tabletop centrifuge. The pellet was saved for protein determination. Supernatants were dried down in a speed vacuum at 4°C. Pellets were also dried down. Last, pellets were resuspended using an amount proportional to the protein amount of insoluble pellet using 1:1 (v/v) acetonitrile/water before analysis. Metabolite extracts were directly measured using untargeted and targeted metabolomic analysis. Protein pellets were dissolved using a 2% SDS buffer containing 10 mM tris (at 95°C) and measured using a commercial bicinchoninic acid (BCA) assay (Thermo Fisher Scientific).

Untargeted metabolomic analysis

Untargeted metabolomic analysis was performed using hydrophilic interaction liquid chromatography (HILIC) fractionation and reversed-phase (RP) chromatography as previously described (*35*). Samples were analyzed on a quadrupole time-of-flight instrument (Impact II, Bruker, Bremen, Germany). The fractionation part was performed by a coupled ultrahigh-performance liquid chromatography (UHPLC) device (Bruker Elute, Bruker, Billerica, MA). Data were acquired over a m/z range of 50 to 1000 Da in positive ion mode. The MS was calibrated using sodium formate (post-run mass calibration). The electrospray source conditions were as follows: end plate offset, 500 V; dry gas temperature, 200°C; drying gas, 6 liters/min; nebulizer, 1.6 bar; and capillary voltage, 3500 V.

A dual fractionation strategy was used to increase metabolome coverage and minimize ion suppression. RP chromatography was done on an ACQUITY BEH C18 column (1.0 × 100 mm, 1.7-µm particle size; Waters Corporation, Milford, MA), and HILIC fractionation was performed using an ACQUITY BEH amide (1.0 × 100 mm, 1.7-µm particle size; Waters Corporation, Milford, MA) column. Flow was 150 µl/min. The gradient for RP was as follows: 99% A for 1 min, 1% A over 9 min, 35% A over 13 min, 60% A over 3 min, and held at 60% A for an additional 1 min. The gradient for HILIC consisted of 1% A for 1 min, 35% A over 13 min, 60% A over 3 min, and held at 60% A for an additional 1 min. The injection volume was 2 µl. For identification, putative molecules of interest were fragmented using three different collision energies (10, 20, and 40 eV) or ramp collision energies (20 to 50 eV).

Metabolite identification and metabolomic data processing

Metabolomic data were converted from .d (Bruker, Bremen, Germany) format into .mzdata format. Metabolomic data processing was performed using the XCMS online platform (*36*) that also performed initial quality controls and multivariate analysis of the data, including principal components analysis, as well as isotope removal and adduct annotation. Primary annotation levels were obtained using the MISA annotation, an in-source fragment annotation algorithm (*9*). Features were considered for multigroup analysis if $q < 0.05$ and maximal intensity was larger than 10,000. Metabolites were identified after obtaining MS2 spectra using the following criteria: Accurate masses, authentic standards, and comparison with spectral databases [primarily METLIN (*37*)] were used to identify compounds. A maximum of 2 ppm (parts per million) of mass error was tolerated. Authentic standard compounds were used for every identified metabolite to determine its identity and to confirm its MS2 spectrum in positive and negative ion mode, as well as its retention time. Data were processed using peak alignment software XCMS online. Hierarchical clustering was performed using Euclidean distance without *K*-means preprocessing. Chemicals and reagents were obtained from Sigma.

Targeted metabolomic analysis

Targeted metabolomic analysis was performed on a triple-quadrupole (QQQ) mass spectrometer (Agilent Triple Quadrupole 6490, San Diego, CA) coupled to a high-performance liquid chromatography (HPLC) system (1290 Infinity, Agilent Technologies) coupled to ion funnel. A ZIC-pHILIC (Sequant column; 2.1 × 150 mm) was used for separation. Cycle time was 500 ms. Collision energies and product ions (MS2 or quantifier and qualifier ion transitions) were optimized. Electrospray ionization source conditions were set as follows: gas temperature, 250°C; gas flow, 12 liters/min; Nebulizer, 20 psi; sheath gas temperature, 350°C; cap voltage, 2000 V; and nozzle voltage, 1000 V. The gradient consisted of buffer A and buffer B. Buffer A was 95:5 H_2O:acetonitrile, 20 mM NH_4OAc, 20 mM NH_4OH (pH 9.4). Buffer B was acetonitrile. The gradient with A/B ratios were as follows: T0, 10:90; T1.5, 10:90; T20, 60:40; T25, off. Five microliters was injected. The used transitions for metabolites can be found in table S2. Metabolite identity was also verified by the addition of deuterated isotope–labeled standards. To quantify oxolipids, the manufacturer's suggested transitions were followed (Cayman Chemical, item no. 192228).

Sample preparation for proteomic analysis

Glomeruli were solubilized in 8 M urea containing 10 mM tris and protease inhibitor (Roche cOmplete) as well as phosphatase inhibitor cocktail 1× (Thermo Fisher Scientific). Protein abundance was determined with the BCA (Thermo Fisher Scientific), and 50 µg of protein was further processed for proteomic analysis. In brief, proteins were reduced using 5 mM dithiothreitol and 10 mM iodoacetamide. Trypsin (Promega, MS grade) was added at a 1:200 (w/w) ratio, and proteins were digested overnight. The next day, digested peptides were acidified and cleaned up using stop and go in-tip cleanup (StageTips).

Sample preparation for phosphoproteomic analysis

Phosphoproteomics of rat glomeruli was essentially performed as previously described (*38*). Glomerular peptides (100 µg) were

subjected to desalting using Oasis HLB columns (Waters). Desalted peptides were dried down and resuspended in 20% acetic acid. Phosphopeptides were enriched using Fe-NTA phosphopeptide enrichment resin columns (Thermo Fisher Scientific) as previously described (*38*), and StageTips cleanup was performed.

MS-based proteomic analysis

Peptides were analyzed on a Quadrupole-Orbitrap mass spectrometer as previously described (*39*). In brief, peptides were separated in a homemade C18 column (50 cm, particle size; Sera-Mag). A nano-LC fractionation was performed before analysis in the mass spectrometer. For both phosphopeptide and peptide samples, a 2.5-hour gradient was used using a binary buffer system consisting of an aqueous and organic phase: buffer A (0.1% formic acid) and buffer B (80% acetonitrile, 0.1% formic acid). Data-dependent acquisition was performed using the following parameters: Automatic gain control (AGC) target for MS1 spectra was 1×10^6. The maximal injection time was 20 ms, and resolution was 70,000 (mass range, 200 to 1200 *m/z*). MS/MS spectra of the top 10 most intense peaks were obtained by higher-energy collisional dissociation fragmentation. MS/MS spectra resolution was set to 35,000 at 200 *m/z*. AGC target was 5×10^5. Maximal injection time was 120 ms. The isolation window was set to 1.3 Th.

Analysis of proteomic data

Proteomic data from different mouse models were performed using MaxQuant v1.6. with the Andromeda search algorithm embedded. Default settings were used such that proteins detected with only one peptide and as a posttranslational modification (site) only were excluded. Peptide spectrum match, protein, and peptide false discovery rate (FDR) were adjusted to <0.01, and a target decoy approach was used against the rat UniProt database (reference proteome) downloaded in January 2017. Match between run option was enabled. Intensity-based quantification (iBAQ) was performed as previously described (*15*). Protein intensities concatenated by the MaxQuant algorithm were quantitatively analyzed using the MaxLFQ algorithm, an algorithm aligning peaks and performing accurate quantification. Phosphopeptide site localization probability was set to be larger than 0.8. Phosphorylation motifs were annotated on the basis of the phosphosite plus (*40*) dataset downloaded in January 2018, and Fisher's exact test was performed for enrichment (FDR value cutoff was smaller than 0.01). Motifs were generated using the iceLogo (*41*) algorithm using rat UniProt database as a reference set.

Bioinformatic integration of glomerular proteomes of models of albuminuria

Quantitative proteomic data were acquired from glomeruli from published mouse models of doxorubicin-induced podocyte injury, the PAN rat and human glomerular data, and primary urinary cells from patients, as well as podocyte-specific proteomic data. These datasets were downloaded from previous publications (*14*–*17*). These data were mapped onto the homologene identifiers in the MGI database downloaded in October 2018 (*42*). Data were $\log_2$-transformed, and the difference between proteinuria and control samples and a *P* value were obtained. These data were normalized by *z* scoring and subjected to hierarchical clustering (Euclidean distance, *K*-means preprocessing), resulting in definition of four major clusters using the Perseus 1.4 framework. Differences in cluster expression were also plotted using boxplots.

Phosphoproteomic network analysis

First, the normalized phosphoproteomic data were compared to the baseline ($t = 0$) to obtain the differential phosphorylation after 7 and 21 days. This analysis was performed by fitting a linear model for each phosphosite and contrast (7 days compared to baseline and 21 days compared to baseline) by using the R package limma (v3.34.9). Statistical significance was estimated using empirical Bayes method from the same package. The kinase-substrate background network was extracted from OmniPath database (as of 15 February 2019) (*43*). Using this previous knowledge along with the differential phosphorylation, the network analysis was performed using PHONEMeS (*10*) implemented with integer linear programming (ILP). This allowed us to extract the phosphorylation cascades from the data at both time points. To run the algorithm, we selected PRKAA1, PRKAA2, and MTOR as starting nodes (proteins), as indicated by the metabolomic data. The *P* value threshold was set to 0.1. The resulting network was visualized using Cytoscape (v3.7.1). The code used to perform the analysis can be found at https://github.com/saezlab/Hypertension_DAHL_rat.

Natural language processing

The IBM Watson (*13*) drug discovery platform was used to extract activating relationships between regulated metabolites (as compounds) and genes. The "Explore a Network" function uses NLP and searches for genes, drugs, conditions, or chemicals to discover a network of relationships supported by evidence found in medical documents and other data sources. Publication bias is corrected through a non-published mechanism using this approach. The dysregulated metabolites were entered as chemicals, and the results were protein-encoding genes associated with the metabolites. The identifications were filtered using a confidence score of at least 86/100 (default setting) and at least three papers showing the relationship. The resulting network was exported and reopened in Cytoscape version 3.6.1 (*44*). Nodes and edges were colored and rearranged as described in the figure legend. The raw data for the network are presented in data file S5.

Statistics

GraphPad Prism v6.00 (GraphPad Software Inc., San Diego, CA, USA) was used for statistical analysis. The quantitative triple quadrupole data were log-transformed and expressed as mean ± SEM after two-tailed *t* tests were carried out. Statistical tests for data without normal distribution (such as a Kruskal-Wallis test) were used for nonnormal distributed data. Comparisons with $P < 0.05$ were generally assigned to be statistically significant and noted on each graph, unless stated otherwise.

SUPPLEMENTARY MATERIALS

stke.sciencemag.org/cgi/content/full/12/611/eaax9760/DC1
Fig. S1. Proteomic alterations in DSS rats.
Fig. S2. Expression analysis of proteins in two canonical pathways.
Fig. S3. Metabolic network modeling of cross-omics data.
Fig. S4. Meta-analysis of proteomic results across different models of proteinuria.
Fig. S5. MS specifics of identified metabolites.
Data file S1. Untargeted metabolomic results.
Data file S2. Targeted metabolomic transitions.
Data file S3. Phosphoproteomic results.
Data file S4. Proteomic results.
Data file S5. Tabular data describing metabolite-protein relationships in Fig. 6C.
Data file S6. Combined proteomic results.

View/request a protocol for this paper from *Bio-protocol*.

REFERENCES AND NOTES

1. E. J. Benjamin, P. Muntner, A. Alonso, M. S. Bittencourt, C. W. Callaway, A. P. Carson, A. M. Chamberlain, A. R. Chang, S. Cheng, S. R. Das, F. N. Delling, L. Djousse, M. S. V. Elkind, J. F. Ferguson, M. Fornage, L. C. Jordan, S. S. Khan, B. M. Kissela, K. L. Knutson, T. W. Kwan, D. T. Lackland, T. T. Lewis, J. H. Lichtman, C. T. Longenecker, M. S. Loop, P. L. Lutsey, S. S. Martin, K. Matsushita, A. E. Moran, M. E. Mussolino, M. O'Flaherty, A. Pandey, A. M. Perak, W. D. Rosamond, G. A. Roth, U. K. A. Sampson, G. M. Satou, E. B. Schroeder, S. H. Shah, N. L. Spartano, A. Stokes, D. L. Tirschwell, C. W. Tsao, M. P. Turakhia, L. B. VanWagner, J. T. Wilkins, S. S. Wong, S. S. Virani; American Heart Association Council on Epidemiology and Prevention Statistics Committee and Stroke Statistics Subcommittee, Heart disease and stroke statistics—2019 update: A report from the American Heart Association. *Circulation* **139**, e56–e528 (2019).
2. J. E. Hall, Renal dysfunction, rather than nonrenal vascular dysfunction, mediates salt-induced hypertension. *Circulation* **133**, 894–906 (2016).
3. T. A. Kotchen, A. W. Cowley, E. D. Frohlich, Salt in health and disease—A delicate balance. *N. Engl. J. Med.* **368**, 1229–1237 (2013).
4. P. T. Brinkkoetter, C. Ising, T. Benzing, The role of the podocyte in albumin filtration. *Nat. Rev. Nephrol.* **9**, 328–336 (2013).
5. M. M. Rinschen, J. Ivanisevic, M. Giera, G. Siuzdak, Identification of bioactive metabolites using activity metabolomics. *Nat. Rev. Mol. Cell Biol.* **20**, 353–367 (2019).
6. C. Guijas, J. R. Montenegro-Burke, B. Warth, M. E. Spilker, G. Siuzdak, Metabolomics activity screening for identifying metabolites that modulate phenotype. *Nat. Biotechnol.* **36**, 316–320 (2018).
7. Chronic Kidney Disease (CKD) Surveillance Project; https://nccd.cdc.gov/ckd/.
8. A. W. Cowley Jr., The genetic dissection of essential hypertension. *Nat. Rev. Genet.* **7**, 829–840 (2006).
9. X. Domingo-Almenara, J. R. Montenegro-Burke, C. Guijas, E. L.-W. Majumder, H. P. Benton, G. Siuzdak, Autonomous METLIN-guided in-source fragment annotation for untargeted metabolomics. *Anal. Chem.* **91**, 3246–3253 (2019).
10. C. D. A. Terfve, E. H. Wilkes, P. Casado, P. R. Cutillas, J. Saez-Rodriguez, Large-scale models of signal propagation in human cells derived from discovery phosphoproteomic data. *Nat. Commun.* **6**, 8033 (2015).
11. J. R. A. Hutchins, W. J. Moore, F. E. Hood, J. S. J. Wilson, P. D. Andrews, J. R. Swedlow, P. R. Clarke, Phosphorylation regulates the dynamic interaction of RCC1 with chromosomes during mitosis. *Curr. Biol.* **14**, 1099–1104 (2004).
12. L. Cottret, D. Wildridge, F. Vinson, M. P. Barrett, H. Charles, M.-F. Sagot, F. Jourdan, MetExplore: A web server to link metabolomic experiments and genome-scale metabolic networks. *Nucleic Acids Res.* **38**, W132–W137 (2010).
13. Y. Chen, J. D. Elenee Argentinis, G. Weber, IBM watson: How cognitive computing can be applied to big data challenges in life sciences research. *Clin. Ther.* **38**, 688–701 (2016).
14. M. M. Rinschen, F. Grahammer, A.-K. Hoppe, P. Kohli, H. Hagmann, O. Kretz, S. Bertsch, M. Höhne, H. Göbel, M. P. Bartram, R. K. Gandhirajan, M. Krüger, P.-T. Brinkkoetter, T. B. Huber, M. Kann, S. A. Wickström, T. Benzing, B. Schermer, YAP-mediated mechanotransduction determines the podocyte's response to damage. *Sci. Signal.* **10**, eaaf8165 (2017).
15. M. M. Rinschen, M. Gödel, F. Grahammer, S. Zschiedrich, M. Helmstädter, O. Kretz, M. Zarei, D. A. Braun, S. Dittrich, C. Pahmeyer, P. Schroder, C. Teetzen, H. Gee, G. Daouk, M. Pohl, E. Kuhn, B. Schermer, V. Küttner, M. Boerries, H. Busch, M. Schiffer, C. Bergmann, M. Krüger, F. Hildebrandt, J. Dengjel, T. Benzing, T. B. Huber, A multi-layered quantitative in vivo expression atlas of the podocyte unravels kidney disease candidate genes. *Cell Rep.* **23**, 2495–2508 (2018).
16. M. Höhne, C. K. Frese, F. Grahammer, C. Dafinger, G. Ciarimboli, L. Butt, J. Binz, M. J. Hackl, M. Rahmatollahi, M. Kann, S. Schneider, M. M. Altintas, B. Schermer, T. Reinheckel, H. Göbel, J. Reiser, T. B. Huber, R. Kramann, T. Seeger-Nukpezah, M. C. Liebau, B. B. Beck, T. Benzing, A. Beyer, M. M. Rinschen, Single-nephron proteomes connect morphology and function in proteinuric kidney disease. *Kidney Int.* **93**, 1308–1319 (2018).
17. M. P. Bartram, S. Habbig, C. Pahmeyer, M. Höhne, L. T. Weber, H. Thiele, J. Altmüller, N. Kottoor, A. Wenzel, M. Krueger, B. Schermer, T. Benzing, M. M. Rinschen, B. B. Beck, Three-layered proteomic characterization of a novel ACTN4 mutation unravels its pathogenic potential in FSGS. *Hum. Mol. Genet.* **25**, 1152–1164 (2016).
18. F. Grahammer, C. Schell, T. B. Huber, The podocyte slit diaphragm--from a thin grey line to a complex signalling hub. *Nat. Rev. Nephrol.* **9**, 587–598 (2013).
19. E. A. Dennis, P. C. Norris, Eicosanoid storm in infection and inflammation. *Nat. Rev. Immunol.* **15**, 511–523 (2015).
20. A. Carrière, M. Cargnello, L.-A. Julien, H. Gao, E. Bonneil, P. Thibault, P. P. Roux, Oncogenic MAPK signaling stimulates mTORC1 activity by promoting RSK-mediated raptor phosphorylation. *Curr. Biol.* **18**, 1269–1277 (2008).
21. B. E. Schaffer, R. S. Levin, N. T. Hertz, T. J. Maures, M. L. Schoof, P. E. Hollstein, B. A. Benayoun, M. R. Banko, R. J. Shaw, K. M. Shokat, A. Brunet, Identification of AMPK phosphorylation sites reveals a network of proteins involved in cell invasion and facilitates large-scale substrate prediction. *Cell Metab.* **22**, 907–921 (2015).
22. M. Schiffer, B. Teng, C. Gu, V. A. Shchedrina, M. Kasaikina, V. A. Pham, N. Hanke, S. Rong, F. Gueler, P. Schroder, I. Tossidou, J.-K. Park, L. Staggs, H. Haller, S. Erschow, D. Hilfiker-Kleiner, C. Wei, C. Chen, N. Tardi, S. Hakroush, M. K. Selig, A. Vasilyev, S. Merscher, J. Reiser, S. Sever, Pharmacological targeting of actin-dependent dynamin oligomerization ameliorates chronic kidney disease in diverse animal models. *Nat. Med.* **21**, 601–609 (2015).
23. S. S. Hayek, K. H. Koh, M. E. Grams, C. Wei, Y.-A. Ko, J. Li, B. Samelko, H. Lee, R. R. Dande, H. W. Lee, E. Hahm, V. Peev, M. Tracy, N. J. Tardi, V. Gupta, M. M. Altintas, G. Garborcauskas, N. Stojanovic, C. A. Winkler, M. S. Lipkowitz, A. Tin, L. A. Inker, A. S. Levey, M. Zeier, B. I. Freedman, J. B. Kopp, K. Skorecki, J. Coresh, A. A. Quyyumi, S. Sever, J. Reiser, A tripartite complex of suPAR, APOL1 risk variants and $\alpha_v\beta_3$ integrin on podocytes mediates chronic kidney disease. *Nat. Med.* **23**, 945–953 (2017).
24. C. Schell, B. Sabass, M. Helmstaedter, F. Geist, A. Abed, M. Yasuda-Yamahara, A. Sigle, J. I. Maier, F. Grahammer, F. Siegerist, N. Artelt, N. Endlich, D. Kerjaschki, H.-H. Arnold, J. Dengjel, M. Rogg, T. B. Huber, ARP3 controls the podocyte architecture at the kidney filtration barrier. *Dev. Cell* **47**, 741–757.e8 (2018).
25. H. Chen, G. Cao, D.-Q. Chen, M. Wang, N. D. Vaziri, Z.-H. Zhang, J.-R. Mao, X. Bai, Y.-Y. Zhao, Metabolomics insights into activated redox signaling and lipid metabolism dysfunction in chronic kidney disease progression. *Redox Biol.* **10**, 168–178 (2016).
26. D.-Q. Chen, G. Cao, H. Chen, C. P. Argyopoulos, H. Yu, W. Su, L. Chen, D. C. Samuels, S. Zhuang, G. P. Bayliss, S. Zhao, X.-Y. Yu, N. D. Vaziri, M. Wang, D. Liu, J.-R. Mao, S.-X. Ma, J. Zhao, Y. Zhang, Y.-Q. Shang, H. Kang, F. Ye, X.-H. Cheng, X.-R. Li, L. Zhang, M.-X. Meng, Y. Guo, Y.-Y. Zhao, Identification of serum metabolites associating with chronic kidney disease progression and anti-fibrotic effect of 5-methoxytryptophan. *Nat. Commun.* **10**, 1476 (2019).
27. D.-Q. Chen, G. Cao, H. Chen, D. Liu, W. Su, X.-Y. Yu, N. D. Vaziri, X.-H. Liu, X. Bai, L. Zhang, Y.-Y. Zhao, Gene and protein expressions and metabolomics exhibit activated redox signaling and wnt/β-catenin pathway are associated with metabolite dysfunction in patients with chronic kidney disease. *Redox Biol.* **12**, 505–521 (2017).
28. H. Chen, L. Chen, D. Liu, D.-Q. Chen, N. D. Vaziri, X.-Y. Yu, L. Zhang, W. Su, X. Bai, Y.-Y. Zhao, Combined clinical phenotype and lipidomic analysis reveals the impact of chronic kidney disease on lipid metabolism. *J. Proteome Res.* **16**, 1566–1578 (2017).
29. Y.-L. Feng, H. Chen, D.-Q. Chen, N. D. Vaziri, W. Su, S.-X. Ma, Y.-Q. Shang, J.-R. Mao, X.-Y. Yu, L. Zhang, Y. Guo, Y.-Y. Zhao, Activated NF-κB/Nrf2 and Wnt/β-catenin pathways are associated with lipid metabolism in CKD patients with microalbuminuria and macroalbuminuria. *Biochim. Biophys. Acta* **1865**, 2317–2332 (2019).
30. S. Chakraborty, S. Galla, X. Cheng, J.-Y. Yeo, B. Mell, V. Singh, B. Yeoh, P. Saha, A. V. Mathew, M. Vijay-Kumar, B. Joe, Salt-responsive metabolite, β-hydroxybutyrate, attenuates hypertension. *Cell Rep.* **25**, 677–689.e4 (2018).
31. D. V. Ilatovskaya, G. Blass, O. Palygin, V. Levchenko, T. S. Pavlov, M. N. Grzybowski, K. Winsor, L. S. Shuyskiy, A. M. Geurts, A. W. Cowley, L. Birnbaumer, A. Staruschenko, A NOX4/TRPC6 pathway in podocyte calcium regulation and renal damage in diabetic kidney disease. *J. Am. Soc. Nephrol.* **29**, 1917–1927 (2018).
32. O. Palygin, V. Levchenko, D. V. Ilatovskaya, T. S. Pavlov, O. M. Pochynyuk, H. J. Jacob, A. M. Geurts, M. R. Hodges, A. Staruschenko, Essential role of Kir5.1 channels in renal salt handling and blood pressure control. *JCI Insight* **2**, 92331 (2017).
33. B. Miller, O. Palygin, V. A. Rufanova, A. Chong, J. Lazar, H. J. Jacob, D. Mattson, R. J. Roman, J. M. Williams, A. W. Cowley, A. M. Geurts, A. Staruschenko, J. D. Imig, A. Sorokin, p66Shc regulates renal vascular tone in hypertension-induced nephropathy. *J. Clin. Invest.* **126**, 2533–2546 (2016).
34. M. R. Späth, M. P. Bartram, N. Palacio-Escat, K. J. R. Hoyer, C. Debes, F. Demir, C. B. Schroeter, A. M. Mandel, F. Grundmann, G. Ciarimboli, A. Beyer, J. N. Kizhakkedathu, S. Brodesser, H. Göbel, J. U. Becker, T. Benzing, B. Schermer, M. Höhne, V. Burst, J. Saez-Rodriguez, P. F. Huesgen, R.-U. Müller, M. M. Rinschen, The proteome microenvironment determines the protective effect of preconditioning in cisplatin-induced acute kidney injury. *Kidney Int.* **95**, 333–349 (2018).
35. J. Ivanisevic, Z.-J. Zhu, L. Plate, R. Tautenhahn, S. Chen, P. J. O'Brien, C. H. Johnson, M. A. Marletta, G. J. Patti, G. Siuzdak, Toward 'omic scale metabolite profiling: A dual separation-mass spectrometry approach for coverage of lipid and central carbon metabolism. *Anal. Chem.* **85**, 6876–6884 (2013).
36. C. A. Smith, E. J. Want, G. O'Maille, R. Abagyan, G. Siuzdak, XCMS: Processing mass spectrometry data for metabolite profiling using nonlinear peak alignment, matching, and identification. *Anal. Chem.* **78**, 779–787 (2006).
37. C. Guijas, J. R. Montenegro-Burke, X. Domingo-Almenara, A. Palermo, B. Warth, G. Hermann, G. Koellensperger, T. Huan, W. Uritboonthai, A. E. Aisporna, D. W. Wolan, M. E. Spilker, H. P. Benton, G. Siuzdak, METLIN: A technology platform for identifying knowns and unknowns. *Anal. Chem.* **90**, 3156–3164 (2018).
38. M. M. Rinschen, C. Pahmeyer, T. Pisitkun, N. Schnell, X. Wu, M. Maaß, M. P. Bartram, T. Lamkemeyer, B. Schermer, T. Benzing, P. T. Brinkkoetter, Comparative phosphoproteomic analysis of mammalian glomeruli reveals conserved podocin C-terminal phosphorylation as a determinant of slit diaphragm complex architecture. *Proteomics* **15**, 1326–1331 (2015).

39. M. M. Rinschen, P. Bharill, X. Wu, P. Kohli, M. J. Reinert, O. Kretz, I. Saez, B. Schermer, M. Höhne, M. P. Bartram, S. Aravamudhan, B. R. Brooks, D. Vilchez, T. B. Huber, R.-U. Müller, M. Krüger, T. Benzing, The ubiquitin ligase Ubr4 controls stability of podocin/MEC-2 supercomplexes. *Hum. Mol. Genet.* **25**, 1328–1344 (2016).
40. P. V. Hornbeck, B. Zhang, B. Murray, J. M. Kornhauser, V. Latham, E. Skrzypek, PhosphoSitePlus, 2014: Mutations, PTMs and recalibrations. *Nucleic Acids Res.* **43**, D512–D520 (2015).
41. D. Maddelein, N. Colaert, I. Buchanan, N. Hulstaert, K. Gevaert, L. Martens, The iceLogo web server and SOAP service for determining protein consensus sequences. *Nucleic Acids Res.* **43**, W543–W546 (2015).
42. C. J. Bult, J. T. Eppig, J. A. Kadin, J. E. Richardson, J. A. Blake; Mouse Genome Database Group, The Mouse Genome Database (MGD): Mouse biology and model systems. *Nucleic Acids Res.* **36**, D724–D728 (2008).
43. D. Türei, T. Korcsmáros, J. Saez-Rodriguez, OmniPath: Guidelines and gateway for literature-curated signaling pathway resources. *Nat. Methods* **13**, 966–967 (2016).
44. P. Shannon, A. Markiel, O. Ozier, N. S. Baliga, J. T. Wang, D. Ramage, N. Amin, B. Schwikowski, T. Ideker, Cytoscape: A software environment for integrated models of biomolecular interaction networks. *Genome Res.* **13**, 2498–2504 (2003).
45. Y. Perez-Riverol, A. Csordas, J. Bai, M. Bernal-Llinares, S. Hewapathirana, D. J. Kundu, A. Inuganti, J. Griss, G. Mayer, M. Eisenacher, E. Pérez, J. Uszkoreit, J. Pfeuffer, T. Sachsenberg, S. Yilmaz, S. Tiwary, J. Cox, E. Audain, M. Walzer, A. F. Jarnuczak, T. Ternent, A. Brazma, J. A. Vizcaíno, The PRIDE database and related tools and resources in 2019: Improving support for quantification data. *Nucleic Acids Res.* **47**, D442–D450 (2019).

Acknowledgments: We would like to thank M. Bruetting for help with the slidescanner and J. Becker for help with the complement (C3) staining. **Funding:** This research was supported by NIH grants R35 HL135749 and P01 HL116264 (to A.S.), Department of Veteran Affairs grant I01 BX004024 (to A.S.), and American Heart Association grants 16EIA26720006 (to A.S.) and 17SDG33660149 (to O.P.). This research was also supported by the Joint Research Center for Computational Biomedicine (JRC- Combine), which is partially funded by Bayer, to J.S.-R. M.M.R. was supported by the DFG (RI2811/1 and RI2811/2). This research was partially funded by NIH grants R35 GM130385, P30 MH062261, P01 DA026146, and U01 CA235493 and by Ecosystems and Networks Integrated with Genes and Molecular Assemblies (ENIGMA), a Scientific Focus Area Program at Lawrence Berkeley National Laboratory for the U.S. Department of Energy, Office of Science, Office of Biological and Environmental Research, under contract number DE-AC02-05CH11231 to G.S. This research benefited from the use of credits from the NIH Cloud Credits Model Pilot, a component of the NIH Big Data to Knowledge (BD2K) program to G.S. **Author contributions:** M.M.R., O.P., A.S., and G.S. conceptualized the study. Investigation and experiments were performed by M.M.R., O.P., C.G., A.P., N.P.-E., X.D.-A., and J.S.-R. Analysis was done by M.M.R., C.G., N.P.-E., R.M.-B., X.D.-A., and J.S.-R. The original draft was written by M.M.R., and writing, review, editing, and final approval were performed by all authors. Resources and supervision were provided by A.S. and G.S. **Competing interests:** The authors declare that they have no competing interests. **Data and materials availability:** The raw MS data of this study have been deposited in PRIDE/ProteomeXchange (*45*) with the following identifiers: PXD007940 (for the proteomic data) and PXD007937 (for the phosphoproteomic data). All other data needed to evaluate the conclusions in the paper are present in the paper or the Supplementary Materials.

Submitted 9 May 2019
Accepted 20 November 2019
Published 10 December 2019
10.1126/scisignal.aax9760

Citation: M. M. Rinschen, O. Palygin, C. Guijas, A. Palermo, N. Palacio-Escat, X. Domingo-Almenara, R. Montenegro-Burke, J. Saez-Rodriguez, A. Staruschenko, G. Siuzdak, Metabolic rewiring of the hypertensive kidney. *Sci. Signal.* **12**, eaax9760 (2019).

Science Signaling

Metabolic rewiring of the hypertensive kidney

Markus M. Rinschen, Oleg Palygin, Carlos Guijas, Amelia Palermo, Nicolas Palacio-Escat, Xavier Domingo-Almenara, Rafael Montenegro-Burke, Julio Saez-Rodriguez, Alexander Staruschenko and Gary Siuzdak

Sci. Signal. **12** (611), eaax9760.
DOI: 10.1126/scisignal.aax9760

Metabolic changes under pressure

Chronic hypertension causes irreversible damage to the kidneys. Rinschen *et al.* performed multi-omics analyses of kidney tissue from rats that spontaneously develop hypertension on a high-salt diet. Their metabolomic analysis revealed that at early disease stages, kidney glomeruli showed various metabolic changes, such as increased lipid breakdown, depletion of branched-chain amino acids, and energy stress. Phosphoproteomic analysis uncovered the activation of the kinase AMPK and the inhibition of the kinase-containing complex mTORC1, as would be expected due to energy stress and depletion of the branched-chain amino acid leucine, respectively. Proteomic analysis demonstrated alterations in the abundance of metabolic enzymes, which correlated with the metabolic changes seen at early disease stages. These results suggest that metabolic interventions could be potentially useful in treating hypertension-induced kidney disease.